



# Amorphous Ni-Nb-Y Alloys as Hydrogen Evolution Electrocatalysts

S. Ghobrial<sup>1</sup> · D. W. Kirk<sup>2</sup> · S. J. Thorpe<sup>1</sup>

Published online: 1 March 2019  
© Springer Science+Business Media, LLC, part of Springer Nature 2019

## Abstract

Ongoing improvements in the performance of anion exchange membranes (AEM) have renewed interest in alkaline water electrolysis for large-scale hydrogen production. New electrocatalysts are required to interface with such AEM water electrolyzers. Ni-Nb-Y amorphous and amorphous-nanocrystalline alloys were prepared by cryomilling and evaluated as electrocatalysts towards the hydrogen evolution reaction. The roles of microstructure and chemistry on catalytic activity were investigated. Characterization by X-ray diffraction and transmission electron microscopy identified Ni<sub>5</sub>Y nanocrystals finely dispersed in an amorphous Ni-Nb-Y matrix among the multiphase alloys. Capacitance measurements near open-circuit potential were used to estimate the electrochemically active surface area (ECSA) in order to elucidate the activity of various catalyst morphologies on an intrinsic basis. Enhanced intrinsic activity from these multiphase structures were found in kinetic data from Tafel and impedance spectroscopic measurements. A multiphase Ni<sub>81.3</sub>Nb<sub>6.3</sub>Y<sub>12.5</sub> catalyst displayed the greatest catalytic activity attributed to the presence of a nanocrystalline Ni<sub>5</sub>Y secondary phase finely dispersed in the Ni-Nb-Y amorphous matrix with increased yttrium content. These preliminary results demonstrate that ball milled Ni-based amorphous-based materials are promising catalysts for electrochemical hydrogen production.

**Keywords** Hydrogen evolution · Amorphous alloy · Mechanical alloying · Rare earth

## Introduction

Increasing reliance on renewable energy sources is driven by the harmful effects of fossil fuel combustion products on public health as well as the growing importance of energy security. Renewable energy sources are inherently intermittent thus requiring conversion to a storable chemical fuel, e.g., hydrogen [1]. One promising solution is to use excess renewable energy to convert water into molecular hydrogen and oxygen via the water electrolysis process [2]. In practice, the industrial application of proton exchange membrane (PEM) water electrolysis is facing several challenges, related to the catalyst: (i) the high cost of highly efficient platinum group metals (PGM), (ii) the global availability of PGM metals, and (iii) the long-term stability of

non-PGM materials [2, 3]. The recent development of anion exchange membranes (AEMs) has renewed interest in alkaline water electrolysis for large-scale production of hydrogen gas. These systems can achieve current densities and form factors comparable to PEM-based systems while enabling the use of non-PGMs as catalyst materials. New electrocatalysts are required to interface with such AEMs in advanced alkaline water electrolyzer (AWE) designs. Ni-based alloys are of a particular interest as catalysts in AWE systems due to their high activity and stability among non-PGM materials. Amorphous alloys have previously been proposed as electrocatalysts due to their unique atomic structure (lacking long-range structural order), which results in electrochemical properties that are particularly suitable for catalysis. These properties include a high density of coordinatively unsaturated sites, greater solute solubility allowing for highly tunable homogeneous short-range order compositions, and a greater stability against surface segregation of solute atoms [4, 5]. Thus far, amorphous alloys have been underutilized as catalysts due to a lack of suitable methods to increase their electrochemically active surface area (ECSA).

One method to facilitate a high ECSA amorphous alloy catalyst morphology is to first produce a heterogeneous microstructure. The heterogeneity enables the selective chemical or

✉ S. Ghobrial  
sam.y.ghobrial@mail.utoronto.ca

<sup>1</sup> Department of Materials Science & Engineering, University of Toronto, Toronto, Ontario M5S 3E4, Canada

<sup>2</sup> Department of Chemical Engineering & Applied Chemistry, University of Toronto, Toronto, Ontario M5S 3E5, Canada

electrochemical dissolution of one phase over another [6]. One such Ni-based system of interest is the Ni-Nb-Y system that has been shown to undergo phase-separation during planar flow casting [7]. Amorphization through such a rapid solidification process targets eutectic or near-eutectic compositions [8]. Deep eutectic compositions have a lower melting temperature lowering the required critical cooling rate and promoting glass formation. Mattern et al. [7] found this system displayed a heterogeneous, two-phase microstructure where both phases were amorphous arising from the preferential partitioning of Y and Nb with Ni. Gerbert et al. [9] studied the Ni-Nb-Y alloy for the HER and found that the as-quenched ribbon demonstrated poor catalytic activity due to its low surface area and the existence of a passive oxide layer. Etching the surface of the phase-separated microstructure (using HF/HNO<sub>3</sub>) led to the selective dissolution of the Y-rich phase, resulting in a high-surface area nanoporous structure with enhanced overall activity. However, a Nb-rich phase remained with poorer intrinsic activity for the HER relative to the Y-rich phase.

Mechanical alloying (via high energy ball milling) and subsequent dealloying can be used to overcome the issue of low ECSA to yield 3D mesoporous and nanoporous amorphous structures. Amorphization through a solid-state process such as mechanical alloying preferentially occurs at compositions corresponding to high-melting intermetallic phases [10]. It is at these intermetallic compositions where the largest kinetic barrier to critical nucleation exists thus enabling the formation of an amorphous phase. Targeting high melting intermetallic compositions on the binary Ni-Nb and Ni-Y phase diagrams identified a novel set of ternary alloy compositions. Fully amorphous and two-phase composite amorphous alloys containing intermetallic phases can both be fabricated. Heterogeneous microstructures have been shown to improve the catalytic activity due to synergistic effects between phases [11–16].

The present work explores the role of microstructure and novel processing to yield unique mechanically alloyed Ni-Nb-Y catalysts. The objective of this work is to study the effect of the chemistry of the amorphous phase, and its synergistic interaction with other microstructural phases present in this system, in optimizing the catalytic activity of the HER through control of the concentration and distribution of yttrium in the ternary alloy system.

## Experimental

### Alloy Synthesis and Structural Characterization

Elemental powders of Ni (Alfa Aesar, 99.9 wt.%), Nb (Alfa Aesar, 99.99 wt.%), and Y (GoodFellow, 99.9 wt.%) were weighed out according to the atomic ratio of the various Ni-Nb-Y alloys. The powder was packed under argon gas in

stainless steel vials with two stainless steel milling balls using a 10:1 ball-to-powder ratio. The powder was mechanically alloyed at 30 Hz for various time periods using a Retch Cryomill with liquid nitrogen cooling. X-ray diffraction (XRD) with Cu K $\alpha$  radiation ( $\lambda = 1.54 \text{ \AA}$ ) was used to analyze the structure of the powder from  $2\theta$  of  $20^\circ$  to  $80^\circ$  with a step size of  $0.05^\circ$  and a measuring time of 3 s per step (Rigaku Miniflex 600). Scanning electron microscopy (SEM, Hitachi SU3500) was performed to image the morphology of the resultant powders. Transmission electron microscopy (TEM) bright-field imaging and selected area diffraction (SAD) were performed using a Hitachi HF3300 at 300 kV. Scanning transmission electron microscopy (STEM) high-angle annular dark-field (HAADF) imaging, local electron diffraction, and electron energy loss spectroscopy (EELS) was performed using a FEI Titan 80-300HB at 200 kV. Bulk chemical compositions of the various alloys produced were verified by inductively couple plasma optical emission spectrometry (ICP-OES, Agilent 700 Series).

### Electrochemical Measurements

The catalyst suspension was prepared by mixing 5.0 mg of powder with 11.2  $\mu\text{L}$  of Nafion 5 wt.% solution (DUPONT D521 NAFION) and 200  $\mu\text{L}$  of isopropanol. The mixture was then sonicated for 15 min before depositing 10  $\mu\text{L}$  onto a 3 mm diameter glassy carbon (GC) electrode (polished to 0.05  $\mu\text{m}$  using colloidal silica). The electrode was then spin-dried in air for at least 1 h. A polycrystalline Ni rod (Alfa Aesar, 99.999%) was also prepared as an electrode. The rod (5 mm diameter) was mounted in epoxy and connected to a copper wire for electrical contact. The exposed surface was polished down to 0.05  $\mu\text{m}$ . All experiments were carried out at  $30.0 \pm 1^\circ\text{C}$  in 1 M KOH electrolyte. The electrolyte solution was prepared from KOH pellets (AnalaR Grade KOH pellets) dissolved in type I water. The aqueous KOH solution was subject to pre-electrolysis using two Pt electrodes for a minimum of 24 h prior to experimentation for the removal of cation impurities, namely Fe. The temperature was maintained by immersing the cell in a water bath. Argon gas was used to deaerate the electrolyte for at least 30 min prior to and then throughout experimentation. A platinum mesh counter electrode and 1 M Hg/HgO reference electrode were used in a three-electrode setup with the catalyst-deposited glassy carbon electrode acting as the working electrode.

All electrochemical measurements were performed using a BioLogic VSP-300 potentiostat. A cathodic potential of  $-1.13 \text{ V}_{\text{Hg/HgO}}$  was first applied for 10 min to reduce any traces of oxy/hydroxides [17]. The working electrode was left to rest for 30 min to achieve a stable open-circuit potential (OCP) prior to subsequent measurements. Solution resistance was estimated by EIS using an AC signal of 5 mV in amplitude and scanning from 100 kHz to 10 mHz.

Electrochemical data was normalized to the electrochemically active surface area (ECSA). The double-layer capacitance ( $C_{dl}$ ) and ECSA of each catalyst was determined following the cyclic voltammetry (CV) technique outlined by McCrory et al. [18]. CV measurements were also performed between  $-0.43$  and  $-1.1$  V<sub>Hg/HgO</sub> at a scan rate of  $100$  mV s $^{-1}$  to investigate surface species during reduction/oxidation processes. Electrochemical impedance spectroscopy (EIS) was conducted at specified DC overvoltages with an AC amplitude of  $5$  mV in the frequency range of  $100$  kHz to  $10$  mHz. Post-processing of EIS data was performed using a method first reported by Ni et al. to transform data to a corresponding time-constant spectra [19]. Tafel measurements were performed using a stepped potentiostatic polarization technique. First, an initial conditioning was applied at  $-1.73$  V<sub>Hg/HgO</sub>. Potential steps of  $\Delta\eta = -20$  mV<sub>Hg/HgO</sub> starting at  $-0.932$  V<sub>Hg/HgO</sub> were applied for a period sufficiently long for a steady-state current density to be established (here  $\Delta t \approx 10$  min). Following the conditioning and between potential steps, “rest” potentials were applied at a voltage negative to OCP to avoid producing any oxides. A rest potential of  $-0.932$  V<sub>Hg/HgO</sub> was applied for  $\Delta t \approx 5$  min.

## Results and Discussion

### Fabrication and Structural Characterization

Analytical techniques (XRD/TEM/SAD) confirmed that the Ni<sub>79.2</sub>Nb<sub>12.5</sub>Y<sub>8.3</sub> alloy, cryogenically ball-milled for  $6$  h, was amorphous. The XRD spectrum showed one broad peak centered at approximately  $44^\circ$  and the lack of any other definitive crystalline peaks suggested that the mechanically alloyed Ni<sub>79.2</sub>Nb<sub>12.5</sub>Y<sub>8.3</sub> material was completely amorphous, see Fig. 1 reproduced with permission [20]. It should be noted that although the XRD spectrum suggested an amorphous structure, fine crystals (embedded in the amorphous matrix)

may have existed below the detection limit of XRD [21]. For example, finely dispersed yttrium oxide (Y<sub>2</sub>O<sub>3</sub>) can easily form during the milling process due to yttrium’s high affinity for oxygen. The minute peak in the XRD spectrum at approximately  $29^\circ$  corresponds to crystalline Y<sub>2</sub>O<sub>3</sub> [22]. TEM and local electron diffraction further elucidated the microstructure (inset Fig. 1). The TEM bright-field image displayed a homogeneous microstructure and the SAD pattern displayed a broad diffuse ring in addition to a set of faint diffraction spots. These features confirmed the existence of an amorphous structure with trace amounts of finely dispersed Y<sub>2</sub>O<sub>3</sub>.

XRD spectra also identified the presence of secondary crystalline phases in the various Ni-Nb-Y amorphous-based alloys, see Fig. 2 reproduced with permission [20]. The multiphase amorphous alloys were produced either by altering the chemical composition, as in the case of catalyst B and D, or by varying the amount of time during mechanical alloying as in the case with catalyst C (milled for  $12$  h). These multiphase alloys were produced in addition to the Ni<sub>79.2</sub>Nb<sub>12.5</sub>Y<sub>8.3</sub> homogeneous amorphous alloy that contained only trace amounts of Y<sub>2</sub>O<sub>3</sub> (Fig. 1). The XRD spectra for all three heterogeneous amorphous alloys (Ni<sub>77.1</sub>Nb<sub>18.8</sub>Y<sub>4.2</sub>, Ni<sub>79.2</sub>Nb<sub>12.5</sub>Y<sub>8.3</sub>, and Ni<sub>81.3</sub>Nb<sub>6.3</sub>Y<sub>12.5</sub>) showed one broad peak centered at approximately  $44^\circ$  (Fig. 2), in a similar manner to the homogenous Ni<sub>79.2</sub>Nb<sub>12.5</sub>Y<sub>8.3</sub> alloy (Fig. 1). In addition to the broad peak that corresponded to the amorphous matrix, the spectra for the multiphase alloys exhibited minor peaks at  $29^\circ$  and  $37^\circ$ . These peaks corresponded to crystalline Y<sub>2</sub>O<sub>3</sub> and Ni<sub>5</sub>Y, respectively [22, 23]. The concentrations of Y<sub>2</sub>O<sub>3</sub> (as indicated by the relative intensity ratio in the XRD spectra) among the heterogeneous amorphous-based alloys were ca. three times greater compared to the homogeneous amorphous Ni<sub>79.2</sub>Nb<sub>12.5</sub>Y<sub>8.3</sub> alloy. The mechanism behind the mechanical alloying process, i.e., the repeated cold-welding and fracturing of particles, resulted in secondary phases which were finely dispersed and nanocrystalline in nature as evidenced by the low-intensity secondary peaks among the similar XRD spectra.

**Fig. 1** XRD spectrum and (inset) TEM bright-field image and SAD pattern of amorphous Ni<sub>79.2</sub>Nb<sub>12.5</sub>Y<sub>8.3</sub> (A)

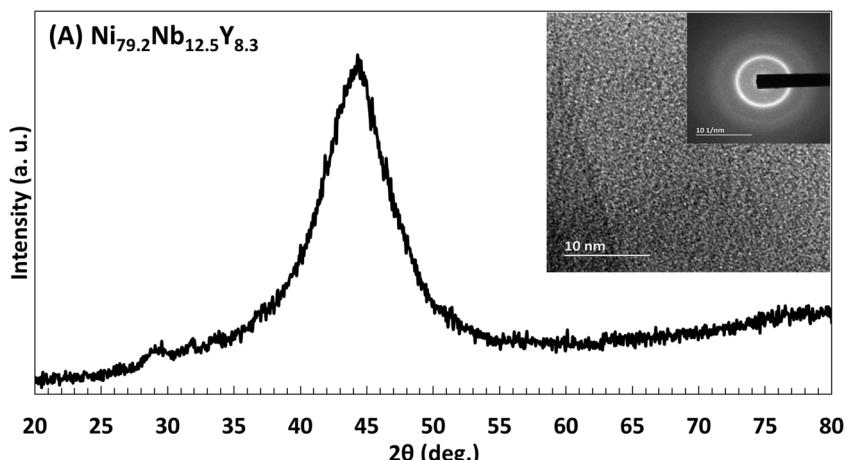
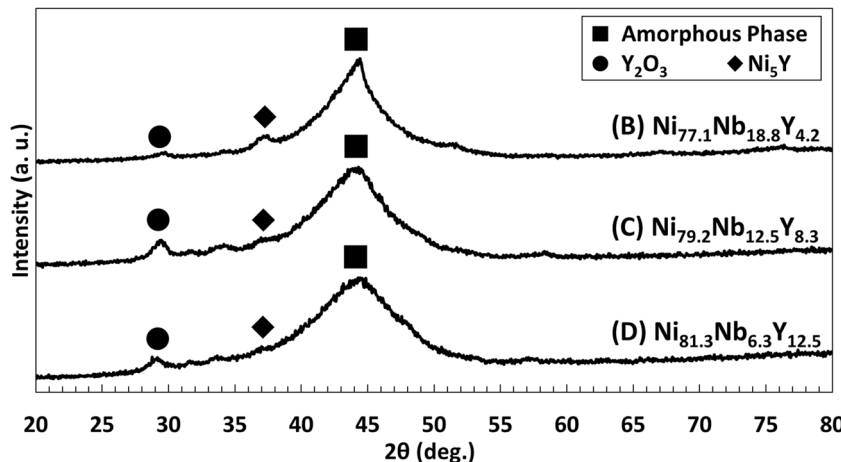


**Fig. 2** XRD spectra for various multiphase Ni-Nb-Y alloys with predominantly amorphous structure and containing secondary crystalline phases (B–D)



Particle morphology was examined using SEM imaging (see Fig. 3). The Ni-Nb-Y alloys all exhibited similar morphology with varying particle size. Based on the SEM images, the average particle sizes were  $26.5 \pm 10.9 \mu\text{m}$ ,  $11.3 \pm 4.3 \mu\text{m}$ ,  $7.0 \pm 2.6 \mu\text{m}$ , and  $14.5 \pm 5.4 \mu\text{m}$  for catalysts A, B, C, and D, respectively. Bulk chemical compositions of the Ni-Nb-Y alloys, as measured by ICP-OES (see Table 1), were found to be in good agreement with the respective nominal compositions.

The multiphase microstructure of the  $\text{Ni}_{81.3}\text{Nb}_{6.3}\text{Y}_{12.5}$  alloy was investigated using STEM-HAADF imaging, local electron diffraction, and STEM-EELS compositional mapping (see Fig. 4). The TEM dark-field image (center of Fig. 4a) acknowledged the heterogenous microstructure with finely dispersed secondary phases. Local electron diffraction in regions 1, 5, and 8 (Fig. 4a) identified the matrix as amorphous as evidenced by the lack of diffraction spots. Regions

2–4, 6, and 7 (Fig. 4a), which corresponds to brighter areas in the dark-field image, confirmed the nanocrystalline secondary phases as evidenced by their clear diffraction spots. EELS elemental mapping around region 2 identified a matrix consisting of Ni, Nb, and Y surrounding the crystalline phase that lacked a clear Nb signal suggesting this phase to be  $\text{Ni}_5\text{Y}$  (Fig. 4b–d). Y-rich phases were also observed (not shown) which lack both Ni and Nb signal, suggesting that these phases were  $\text{Y}_2\text{O}_3$ . Quantification of EELS intensities using a principal component analysis method and a Hartree-Slater cross-sectional model found Ni-Y secondary phases to have  $80.4 \pm 5.7$  at.% Ni and  $19.7 \pm 5.7$  at% Y, which agreed well with the atomic composition of  $\text{Ni}_5\text{Y}$ , which is 83.3 at.% Ni and 16.7 at.% Y. Select Y-rich phases were found to have  $61.7 \pm 10.4$  at.% O,  $34.8 \pm 11.0$  at.% Y, and  $3.45 \pm 0.7$  at.% Ni, this agreed well with the atomic composition of  $\text{Y}_2\text{O}_3$ , which is

**Fig. 3** SEM images of Ni-Nb-Y powder catalysts A, B, C, and D

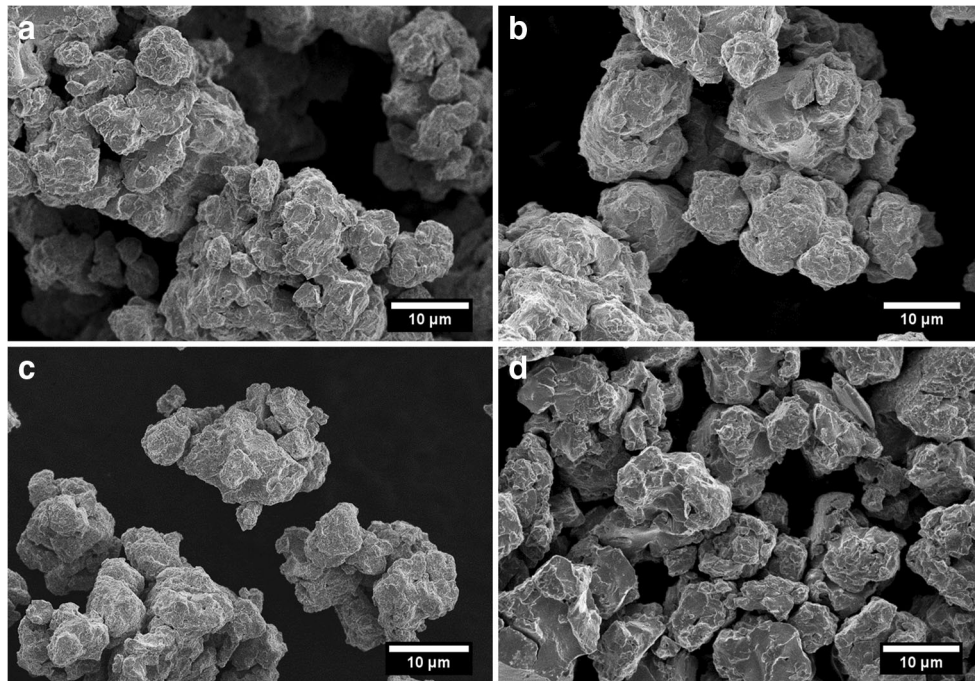


**Table 1** Chemical composition of electrocatalysts measured by ICP-OES

Catalyst		Ni (at.%)	Nb (at.%)	Y (at.%)
A ( $\text{Ni}_{79.2}\text{Nb}_{12.5}\text{Y}_{8.3}$ )	Nominal	79.2	12.5	8.3
	ICP-OES	$81.1 \pm 0.2$	$11.6 \pm 0.1$	$7.2 \pm 0.1$
B ( $\text{Ni}_{77.1}\text{Nb}_{18.8}\text{Y}_{4.2}$ )	Nominal	77.1	18.8	4.2
	ICP-OES	$79.2 \pm 0.2$	$17.2 \pm 0.1$	$3.6 \pm 0.1$
C ( $\text{Ni}_{79.2}\text{Nb}_{12.5}\text{Y}_{8.3}$ )	Nominal	79.2	12.5	8.3
	ICP-OES	$81.0 \pm 0.1$	$11.6 \pm 0.1$	$7.5 \pm 0.1$
D ( $\text{Ni}_{81.3}\text{Nb}_{6.3}\text{Y}_{12.5}$ )	Nominal	81.3	6.3	12.5
	ICP-OES	$82.5 \pm 0.1$	$5.7 \pm 0.1$	$11.9 \pm 0.2$

40 at.% Y and 60 at.% O. It is important to note that the matrix could not be quantified accurately due to the low concentration of Nb; however, EELS mapping did show a rather homogeneous distribution of Ni, Nb, and Y. Summarized in Table 2 are the nominal compositions and the phases observed (by XRD and/or STEM analysis) in the various Ni-Nb-Y alloys.

### Electrochemical Characterization of Activity Towards the HER

The amorphous  $\text{Ni}_{79.2}\text{Nb}_{12.5}\text{Y}_{8.3}$  alloy (A) exhibited improved intrinsic catalytic performance compared to nickel.

**Table 2** Phases present in the Ni-Nb-Y amorphous-based catalysts

Catalyst	Nominal composition	Phases present
A	$\text{Ni}_{79.2}\text{Nb}_{12.5}\text{Y}_{8.3}$	Amorphous, $\text{Y}_2\text{O}_3$ (trace)
B	$\text{Ni}_{77.1}\text{Nb}_{18.8}\text{Y}_{4.2}$	Amorphous, $\text{Ni}_5\text{Y}$ , $\text{Y}_2\text{O}_3$
C	$\text{Ni}_{79.2}\text{Nb}_{12.5}\text{Y}_{8.3}$	Amorphous, $\text{Ni}_5\text{Y}$ , $\text{Y}_2\text{O}_3$
D	$\text{Ni}_{81.3}\text{Nb}_{6.3}\text{Y}_{12.5}$	Amorphous, $\text{Ni}_5\text{Y}$ , $\text{Y}_2\text{O}_3$

The addition of minor secondary crystalline phases (found in catalysts B, C, and D), namely  $\text{Ni}_5\text{Y}$ , resulted in even greater intrinsic performance, see Fig. 5. The corresponding electrochemical properties are summarized in Table 3. Ni as well as the Ni-based alloys displayed two Tafel regimes which are characteristic of high surface area Ni catalysts [24]. The Tafel values from the first regime were between 130 and 150 mV indicative that the HER reaction followed the Volmer–Heyrovsky mechanism with the Volmer (adsorption) reaction as the rate-determining step [25]. The improved catalytic activity of the amorphous  $\text{Ni}_{79.2}\text{Nb}_{12.5}\text{Y}_{8.3}$  alloy (A) over Ni is largely caused by the synergistic effects of alloying transition metals according to the Brewer–Engel valence-bond theory [26]. Specifically, proper alloying of hyper-d-electronic elements (Ni) with hypo-d-electronic elements (Nb, Y) results in a significant change in bond strength affecting the electronic density, intermetallic stability, and catalytic

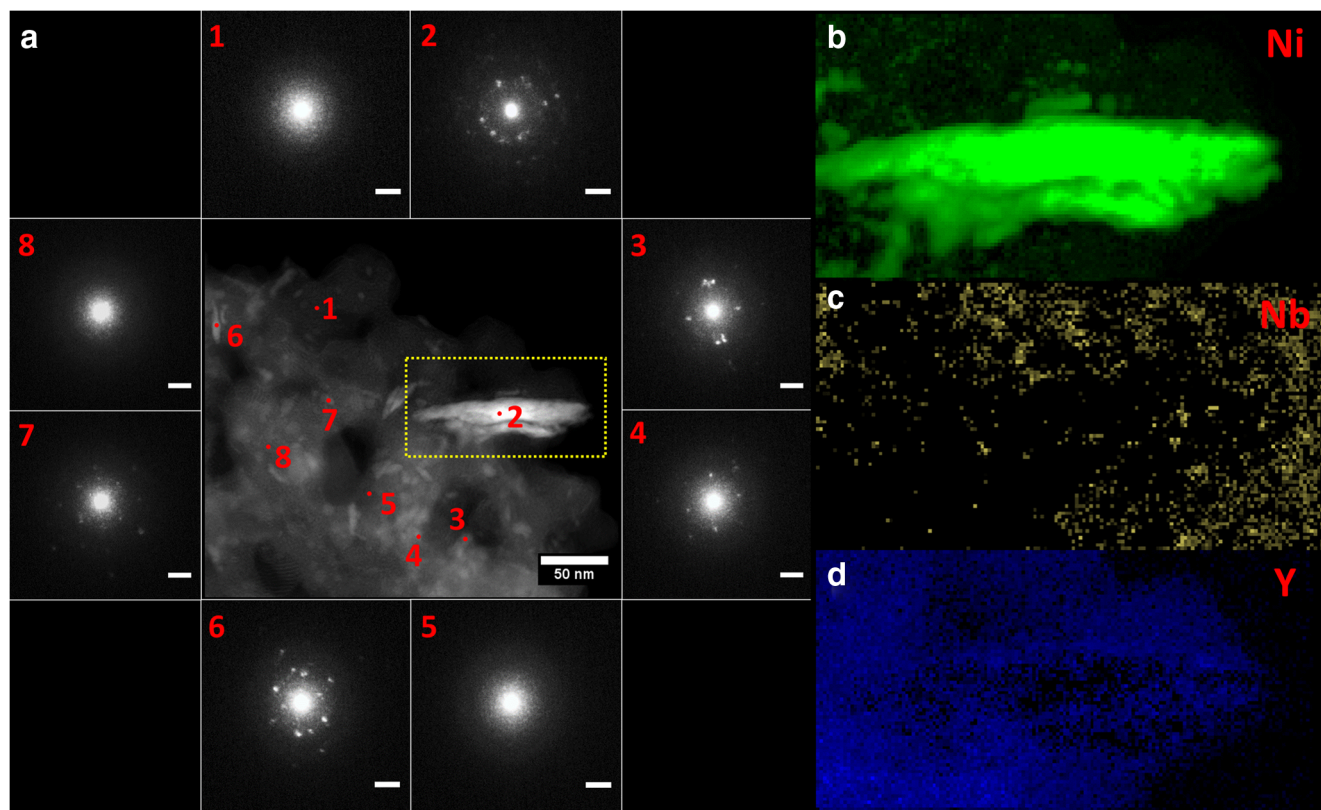


**Fig. 4** **a** STEM-HAADF characterization of catalyst D ( $\text{Ni}_{81.3}\text{Nb}_{6.3}\text{Y}_{12.5}$ ) and corresponding local electron diffraction patterns (scale bars equal  $5 \text{ nm}^{-1}$ ). EELS elemental mapping near region 2 of **b** Ni, **c** Nb, and **d** Y

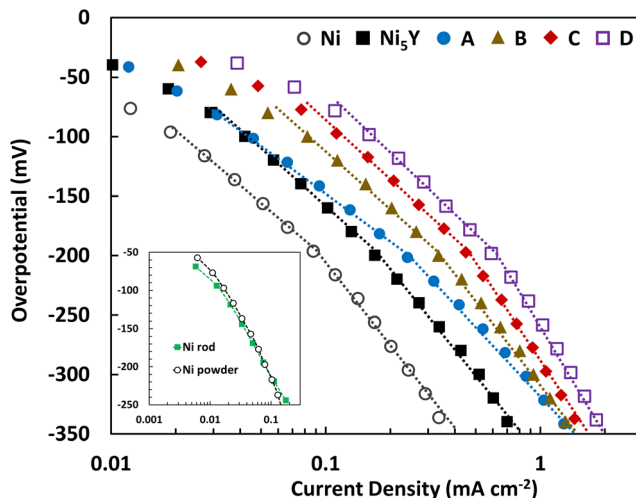


**Fig. 5** Tafel measurements for the Ni-Nb-Y catalysts (A, B, C and D), Ni and  $\text{Ni}_5\text{Y}$  powder supported on GC in 1 M KOH at 30 °C. Inset figure compares Tafel measurements from polished Ni rod and Ni powder supported on GC. Current densities were normalized to the ECSA

activity [27]. Several authors have shown that Ni-based alloys containing rare-earth (RE) elements (La, Y, Sm, Ce, etc.) are particularly active [12, 13, 16, 27–29]. In the case of the phase-separated amorphous Ni-Nb-Y alloy by Gerbert et al., the enhanced activity of the nanoporous catalyst (by selective dissolution of the Y-rich phase) was mainly attributed to the residual Y-rich phase [9].

Catalysts (B), (C), and (D) all contained a significant fraction of  $\text{Ni}_5\text{Y}$  within their amorphous matrix and all exhibited higher catalytic activity than either pure Ni or catalyst (A). In order to elucidate this behavior, crystalline  $\text{Ni}_5\text{Y}$  was also tested for its intrinsic electrochemical properties. The intermetallic compound was cast by vacuum arc-melting of elemental powders of Ni and Y on a water-cooled copper hearth followed by subsequent milling to produce a powder. Although catalyst A contained a lower concentration of Y than the crystalline  $\text{Ni}_5\text{Y}$  catalyst, it exhibited lower Tafel values and a higher catalytic activity overall. This higher activity hints at faster reaction kinetics on the amorphous alloy's surface over its crystalline counterpart.

The Ni-Nb-Y multiphase catalysts (B, C, and D) displayed higher catalytic activity than the homogeneous amorphous

catalyst (A). The improvement in catalytic activity was not only evident between catalysts of the same chemical composition, in which catalyst C displayed an exchange current density that was almost three times higher than catalyst A, but also apparent regarding a catalyst with a lower overall yttrium concentration (i.e., catalyst B), see Table 3. The higher activity among the multiphase catalysts, compared to the  $\text{Ni}_5\text{Y}$  and the amorphous  $\text{Ni}_{79.2}\text{Nb}_{12.5}\text{Y}_{8.3}$  (A) catalysts (i.e., the constituent phases), indicated a possible synergistic effect from the multiphase structure, particularly, the presence of the secondary crystalline  $\text{Ni}_5\text{Y}$  phase. Note that the increase in yttrium concentration did not result in a greater  $\text{Ni}_5\text{Y}$  concentration (according to the relative intensity of the  $\text{Ni}_5\text{Y}$  peak in the XRD spectra), so any addition or depletion of yttrium was likely due to Y partitioned to the amorphous matrix phase rather than the  $\text{Ni}_5\text{Y}$  concentration. Catalyst D was the most active catalyst with an exchange current density that was seven times greater than Ni and almost four times greater than catalyst A. This improvement in performance was attributed to the higher overall yttrium concentration (within the amorphous matrix phase) in addition to the presence of  $\text{Ni}_5\text{Y}$ .

It should be noted that the intrinsic activity (Tafel measurements with current density normalized to the ECSA) of polished Ni rod and Ni powder supported on GC were similar (see inset Fig. 5). These measurements suggest that the double-layer capacitance measurements enabled a reasonable assessment of the ECSA regardless of the catalyst morphology, thus sufficiently capturing the intrinsic activity.

CV measurements between  $-1.1$  and  $-0.4$  V<sub>Hg/HgO</sub> were also performed to provide insight of surface speciation during redox processes (see Fig. 6). CV profiles of Ni and the multiphase catalyst D ( $\text{Ni}_{81.3}\text{Nb}_{6.3}\text{Y}_{12.5}$ ) both exhibited two peaks pertaining to the oxidation and reduction of  $\alpha\text{-Ni(OH)}_2$ , as observed with other Ni-based materials [30, 31]. In comparison, the CV measurements on the GC substrate did not exhibit any redox peak nor was the onset of the HER observed.

Earlier work by Baiker [32, 33] and Yamashita [34] reported exceptional catalytic activity from amorphous alloys that had undergone well-defined heat treatments to include controlled amounts of crystalline phases. The amorphous precursor material ensured the formation of highly active states via

**Table 3** Electrochemical behavior of prepared catalysts tested in 1 M KOH at 30 °C. Current densities were normalized to the ECSA

Catalyst	OCP (mV <sub>Hg/HgO</sub> )	Tafel (1) (mV dec <sup>-1</sup> )	Tafel (2) (mV dec <sup>-1</sup> )	$i_0 \times 10^{-3}$ (mA cm <sup>-2</sup> )	$\eta_j = 0.1$ mA cm <sup>-2</sup> (mV)	$C_{dl}/A_{geo}$ (mF cm <sup>-2</sup> )	RF
Ni	$-895 \pm 0.4$	$-143 \pm 1$	$-242 \pm 3$	$3.6 \pm 0.1$	$210 \pm 3$	$10.5 \pm 1$	$262 \pm 21$
$\text{Ni}_5\text{Y}$	$-911 \pm 0.02$	$-148 \pm 9$	$-223 \pm 14$	$7.56 \pm 1.0$	$158 \pm 4$	$5.5 \pm 0.4$	$136 \pm 9$
A	$-913 \pm 1.8$	$-132 \pm 2$	$-209 \pm 6$	$7.2 \pm 1.0$	$150 \pm 13$	$2.3 \pm 0.4$	$57 \pm 10$
B	$-910 \pm 1.8$	$-141 \pm 2$	$-235 \pm 6$	$13.9 \pm 1.6$	$119 \pm 6$	$2.3 \pm 0.2$	$58 \pm 6$
C	$-914 \pm 1.5$	$-149 \pm 3$	$-277 \pm 8$	$20.6 \pm 0.3$	$93 \pm 2$	$2.9 \pm 0.4$	$73 \pm 9$
D	$-914 \pm 0.8$	$-154 \pm 4$	$-282 \pm 6$	$27.5 \pm 3.7$	$80 \pm 5$	$3.4 \pm 0.3$	$85 \pm 7$

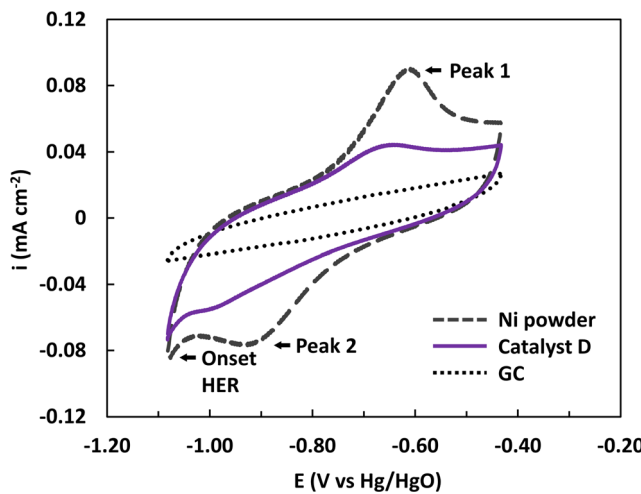


**Fig. 6** CV profiles of Ni, catalyst D ( $\text{Ni}_{81.3}\text{Nb}_{6.3}\text{Y}_{12.5}$ ) and the GC substrate taken in 1 M KOH at 30 °C. Current densities were normalized to the ECSA

the extremely large interfacial area existing between the finely dispersed crystalline phase and the amorphous matrix [5, 35]. Such large interfacial areas have been shown to have higher selectivity and faster diffusion kinetics for hydrogen [35, 36]. Heterogeneous crystalline microstructures can also have a strong influence on catalytic activity towards the HER [11–16, 37, 38]. The enhanced catalytic activity of a composite Ni-Co-LaNi<sub>5</sub> over Ni-Co coating was attributed to both the

intrinsic activity and the favorable hydrogen adsorption properties of the incorporated LaNi<sub>5</sub> particles [38]. Similarly, a multiphase Ni-Co-Y crystalline catalyst displayed greater catalytic activity than the constituent phases indicating a synergistic effect for the HER [12]. The synergy was attributed to the “hydrogen spillover effect,” which involved the fast migration of adsorbed hydrogen between the constituent phases and lead to an improved overall surface coverage [39]. Among the Ni-RE multiphase alloys, a pronounced synergistic effect was observed with alloys containing Ni<sub>5</sub>RE primary crystals as opposed to simply Ni [16, 37].

The improved catalytic activity demonstrated by the multiphase Ni-Nb-Y catalysts in this study is consistent with the above observation and can be attributed to the presence of the highly dispersed secondary crystalline Ni<sub>5</sub>Y phase within an amorphous matrix. In order to provide further evidence of the synergistic effect, EIS was performed on each alloy and Ni<sub>5</sub>Y and the results analyzed in the time-constant domain.

Trends in the kinetic data from EIS measurements agreed with the data from potentiostatic polarization measurements. AC impedance data displayed only one semicircle in the Nyquist impedance plots at the measured overpotentials. This behavior indicated kinetics-controlled charge-transfer reactions, see Fig. 7. The charge-transfer resistance ( $R_{ct}$ ), which relates to the efficiency for the HER reaction, was obtained directly from the Nyquist plot, as the real impedance at low

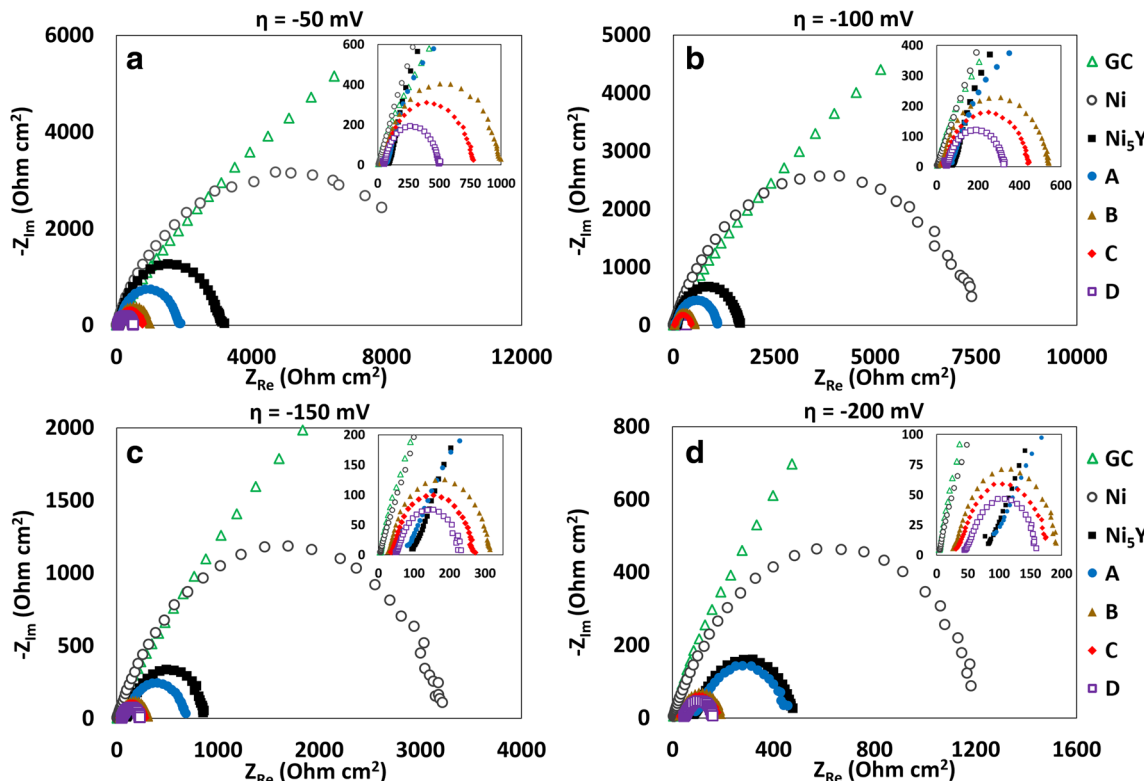


**Fig. 7** Nyquist plots for the HER on GC substrate, Ni, Ni-Nb-Y, and Ni<sub>5</sub>Y catalysts at selected overpotentials: **a** – 50, **b** – 100, **c** – 150, and **d** – 200 mV. Impedance values were normalized to the ECSA

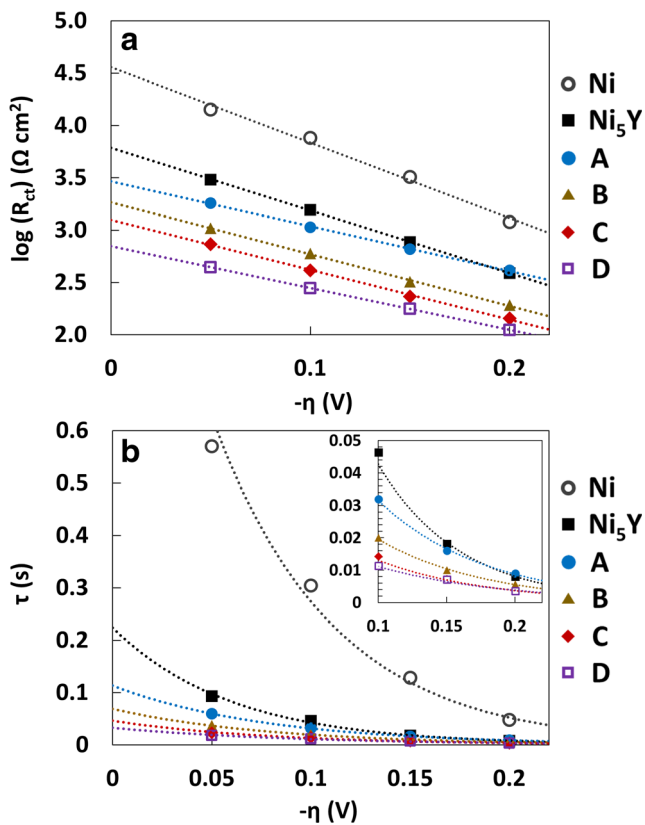


**Fig. 8** **a** Logarithm of  $R_{ct}$  for the HER as a function of overpotential normalized to the ECSA. **b** Time-constant dependence on overpotential for Ni,  $\text{Ni}_5\text{Y}$ , and Ni-Nb-Y catalysts

frequency is equal to the solution resistance ( $R_s$ ) plus the  $R_{ct}$  [40]. As expected, the multiphase catalysts (B, C, and D) all showed significantly lower  $R_{ct}$  values over the measured potential range. Catalyst D ( $\text{Ni}_{81.3}\text{Nb}_{6.3}\text{Y}_{12.5}$ ) displayed the lowest  $R_{ct}$  overall, see Fig. 8a. The glassy carbon substrate exhibited only capacitive behavior in the measured potential and frequency range.

The time-constant ( $\tau = R_{ct} \times C_{dl}$ ) is another kinetic parameter from EIS measurements that can be evaluated. Lower  $\tau$  values indicate an enhanced electrocatalytic activity as it characterizes the relaxation rate of the electrode after a potential is applied [41]. Time-constant values can be determined by fitting the EIS data to an equivalent electrical circuit (EEC), the challenge remains in choosing an equivalent circuit that is

based on a valid system model. Several EECs have been used for the interpretation of EIS data of HER catalysts [42–44]. Simple equivalent circuits have limitations with their application to more complex systems with distributed or heterogeneous properties. Significant surface heterogeneities can lead to changes in local electrochemical properties that result in a time-constant distribution [45, 46]. A data analysis method, developed by Ni et al., was used to further analyze the EIS data by transforming them into their corresponding time-constant spectra. This analysis does not require an explicit EEC [19]. The multiphase catalysts (B, C, and D) displayed lower  $\tau$  values over the measured potential range compared to the homogenous amorphous catalyst (A), Ni, and the  $\text{Ni}_5\text{Y}$  catalyst, while catalyst D displayed the lowest overall  $\tau$  values, see Fig. 8b. The trends in the kinetic data from EIS measurements (i.e.,  $R_{ct}$ ,  $\tau$ ) were further evidence of enhanced intrinsic activity resulting from the multiphase catalysts.  $R_{ct}$  and  $\tau$  values, for catalyst D, extracted using the time-constant spectrum transformation method show good agreement with values obtained by fitting the data to a modified Randle's EEC (see Table 4). The other catalysts evaluated (i.e., A, B, C, and  $\text{Ni}_5\text{Y}$ ) also compare well (not shown).

An insight into the structural morphology of the Ni-Nb-Y catalysts was gained from the electrochemical data reported in Table 3. The ECSA was determined by dividing the  $C_{dl}$  (mF) by a specific capacitance value equal to  $0.040 \text{ mF cm}^{-2}$  for a smooth Ni surface in  $0.5 \text{ M KOH}$  [47]. Roughness factor (RF) values were calculated by dividing the ECSA by the geometric area of the glassy carbon electrode ( $A_{geo} \approx 0.0707 \text{ cm}^2$ ). Catalysts B through D exhibited similar  $C_{dl}$  values that increased slightly with increasing Y content in the amorphous matrix of the alloy independent of the volume fraction of finely dispersed  $\text{Ni}_5\text{Y}$  secondary phases into the amorphous matrix (Fig. 2). The experimental results herein support the hypothesis of enhanced intrinsic activity associated with the multiphase catalyst structure (B, C, and D) compared to catalyst (A). This multiphase structure (by way of the interface) exhibited higher selectivity for  $\text{H}_{ads}$  species and facilitated H-H recombination improving the overall HER kinetics. Figure 9 is a schematic of  $\text{H}_{ads}$  migration towards the interface between the amorphous matrix and the  $\text{Ni}_5\text{Y}$  nanocrystalline phase.

**Table 4** Comparison of EIS kinetic parameters for catalyst D

Overpotential (mV)	Modeling using $\tau$ -spectrum Transformation		Modeling using modified Randle's cell EEC	
	Log $R_{ct}$ ( $\Omega \text{ cm}^2$ )	$\tau$ (ms)	Log $R_{ct}$ ( $\Omega \text{ cm}^2$ )	$\tau$ (ms)
−50	2.65	18.2	2.64	19.4
−100	2.45	11.4	2.43	11.2
−150	2.25	7.10	2.27	6.25
−200	2.04	3.54	2.05	3.29

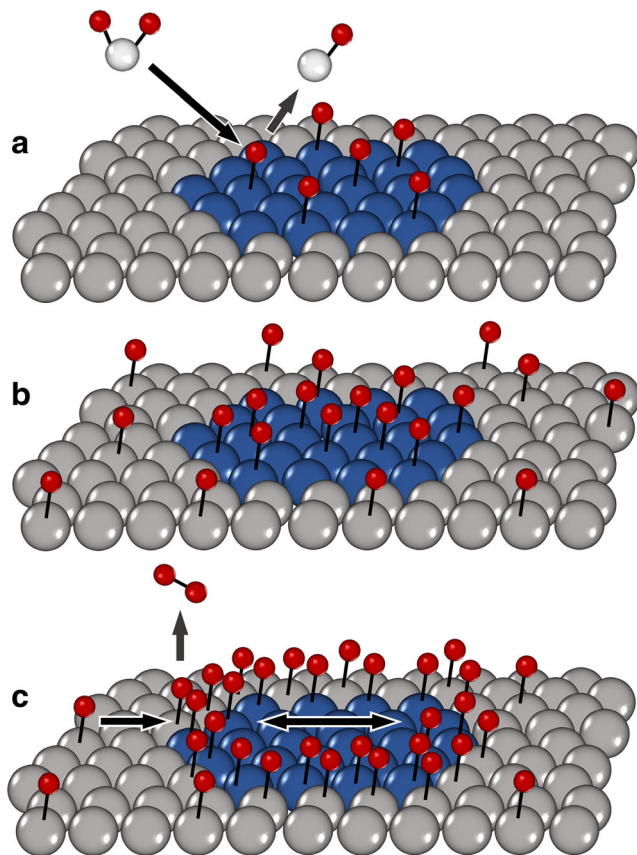


**Fig. 9** Schematic representation of the HER process on multiphase amorphous-crystalline surface (amorphous matrix in gray, crystalline Ni<sub>5</sub>Y secondary phase in blue). **a** Preferential H-adsorption on Ni<sub>5</sub>Y phase, leading to **b** higher surface coverage and **c** H<sub>ads</sub> migration towards the amorphous-crystalline interface facilitating H-H recombination

## Conclusion

The multiphase Ni<sub>81.3</sub>Nb<sub>6.3</sub>Y<sub>12.5</sub> catalyst showed enhanced intrinsic activity towards the HER. Potentiostatic polarization and EIS measurements support the notion of synergistic effects owing to the heterogeneous structure of the alloy. The enhanced catalytic activity was attributed to the combination of the Ni<sub>5</sub>Y intermetallic phase finely dispersed in the yttrium-rich Ni-based amorphous matrix as evidenced by in-depth TEM studies. The multiphase structure enabled improved H<sub>ads</sub> surface coverage due to the large interfacial area and enhanced hydrogen diffusion kinetics on the amorphous-crystalline composite surface.

Multiphase catalyst structures have previously been shown to enhance catalytic activity. The results herein provide further evidence that a multiphase structure in amorphous-based alloys prepared by mechanical alloying can improve performance specifically towards the HER in AWE. The mechanical alloying process can be used to produce highly tunable chemical compositions where the inclusion of finely dispersed secondary crystalline phases

resulted in enhanced catalytic activity. Preliminary electrochemical measurements demonstrate that mechanically alloyed Ni-based amorphous-based materials are promising catalysts for electrochemical hydrogen production.

**Acknowledgments** This work was supported by the University of Toronto, Dept. of Materials Science and Engineering, as well as the Surface Engineering and Electrochemistry (SEE) Research Group. They also acknowledge the assistance from Prof. T. Bender in the Department of Chemical Engineering and Applied Chemistry at the University of Toronto for the use of their laboratory equipment. The authors acknowledge the integral structural characterization work by Dr. S. Prabhudev (Canadian Centre for Electron Microscopy) and Dr. G. Botton (Canada Research Chair in Electron Microscopy of Nanoscale Materials, Dept. of Materials Science and Engineering, McMaster University). The TEM research described in this paper was performed at the Canadian Centre for Electron Microscopy at McMaster University, which is supported by NSERC and other government agencies.

**Funding** The authors gratefully acknowledge the financial support from the Natural Science and Engineering Research Council of Canada (NSERC Discovery Frontiers Grant) through the Engineered Nickel Catalysts for Electrochemical Clean Energy project administered from Queen's University and supported by Grant No. RGPNM 477963-2015.

**Publisher's Note** Springer Nature remains neutral with regard to jurisdictional claims in published maps and institutional affiliations.

## References

1. N.S. Lewis, D.G. Nocera, Powering the planet: Chemical challenges in solar energy utilization. *Proc. Natl. Acad. Sci.* **103**(43), 15729–15735 (2006)
2. Z.W. Seh, J. Kibsgaard, C.F. Dickens, I. Chorkendorff, J.K. Nørskov, T.F. Jaramillo, Combining theory and experiment in electrocatalysis: Insights into materials design. *Science* **355**(146), eaad4998 (2017)
3. R. Subbaraman, D. Tripkovic, K.C. Chang, D. Strmenik, A.P. Paulikas, P. Hirunsit, M. Chan, J. Greeley, V. Stamenkovic, N.M. Markovic, Trends in activity for the water electrolyser reactions on 3d M(Ni,Co,Fe,Mn) hydr(oxy)oxide catalysts. *Nat. Mater.* **11**(6), 550–557 (2012)
4. J.-F. Deng, H. Li, W. Wang, Progress in design of new amorphous alloy catalysts. *Catal. Today* **51**(1), 113–125 (1999)
5. A. Molnár, G.V. Smith, M. Bartók, *Adv. Catal.* **36**, 329 (1989)
6. D.H. Kim, W.T. Kim, E.S. Park, N. Mattern, J. Eckert, Phase separation in metallic glasses. *Prog. Mater. Sci.* **58**(8), 1103–1172 (2013)
7. N. Mattern, U. Kühn, A. Gebert, T. Gemming, M. Zinkevich, H. Wendrock, L. Schultz, Microstructure and thermal behavior of two-phase amorphous Ni–Nb–Y alloy. *Scr. Mater.* **53**(3), 271–274 (2005)
8. W.H. Wang, C. Dong, C.H. Shek, Bulk metallic glasses. *Mater. Sci. Eng. R Reports* **44**(2–3), 45–89 (2004)

9. A. Gebert, N. Mattern, U. Kühn, J. Eckert, L. Schultz, Electrode characteristics of two-phase glass-forming Ni–Nb–Y alloys. *Intermetallics* **15**(9), 1183–1189 (2007)
10. W.L. Johnson, Thermodynamic and kinetic aspects of the crystal to glass transformation in metallic materials. *Prog. Mater. Sci.* **30**(2), 81–134 (1986)
11. J.M. Jaksic, M.V. Vojnovic, N.V. Krstajic, Kinetic analysis of hydrogen evolution at Ni–Mo alloy electrodes. *Electrochim. Acta* **45**(25–26), 4151–4158 (2000)
12. F. Rosalbino, S. Delsante, G. Borzone, E. Angelini, Correlation of microstructure and catalytic activity of crystalline Ni–Co–Y alloy electrode for the hydrogen evolution reaction in alkaline solution. *J. Alloys Compd.* **429**(1–2), 270–275 (2007)
13. F. Rosalbino, S. Delsante, G. Borzone, E. Angelini, Electrocatalytic behaviour of Co–Ni–R (R=Rare earth metal) crystalline alloys as electrode materials for hydrogen evolution reaction in alkaline medium. *Int. J. Hydrol. Energy* **33**(22), 6696–6703 (2008)
14. F. Rosalbino, D. Macciò, A. Saccone, E. Angelini, S. Delfino, Fe–Mo–R (R = rare earth metal) crystalline alloys as a cathode material for hydrogen evolution reaction in alkaline solution. *Int. J. Hydrol. Energy* **36**(3), 1965–1973 (2011)
15. D.M.F. Santos, C.A.C. Sequeira, D. Macciò, A. Saccone, J.L. Figueiredo, Platinum–rare earth electrodes for hydrogen evolution in alkaline water electrolysis. *Int. J. Hydrol. Energy* **38**(8), 3137–3145 (2013)
16. D.M.F. Santos, L. Amaral, B. Sljukic, D. Macciò, A. Saccone, C.A.C. Sequeira, *J. Electrochem. Soc.* **161**, 386 (2014)
17. R. Simpraga, B.E. Conway, Realization of monolayer levels of surface oxidation of nickel by anodization at low temperatures. *J. Electroanal. Chem.* **280**(2), 341–357 (1990)
18. C.C.L. McCrory, S. Jung, I.M. Ferrer, S.M. Chatman, J.C. Peters, T.F. Jaramillo, Benchmarking hydrogen evolving reaction and oxygen evolving reaction electrocatalysts for solar water splitting devices. *J. Am. Chem. Soc.* **137**(13), 4347–4357 (2015)
19. Q. Ni, D.W. Kirk, S.J. Thorpe, Interpreting impedance spectra in the time constant domain: Application to the characterization of passive films. *ECS Trans.* **66**(27), 15–23 (2015)
20. S. Ghobrial, D.W. Kirk, S.J. Thorpe, Electrocatalytic activity of amorphous Ni–Nb–Y alloys for the HER in alkaline water electrolysis. *ECS Trans.* **85**(11), 107–117 (2018)
21. C. Suryanarayana, A. Inoue, *Bulk metallic glasses* (CRC Press, Boca Raton, 2011)
22. S. Katagiri, N. Ishizawa, A new high temperature modification of face-centered cubic Y<sub>2</sub>O<sub>3</sub>. *Powder Diffract.* **8**(01), 60 (1993)
23. A.E. Dwight, *Trans. Am. Soc. Met.* **53**, 479 (1961)
24. J. Van Drunen, B.K. Pilapil, Y. Makonnen, D. Beauchemin, B.D. Gates, G. Jerkiewicz, Electrochemically active nickel foams as support materials for nanoscopic platinum electrocatalysts. *ACS Appl. Mater. Interfaces* **6**(15), 12046–12061 (2014)
25. J.O.M. Bockris, S. Srinivasan, Elucidation of the mechanism of electrolytic hydrogen evolution by the use of H-T separation factors. *Electrochim. Acta* **9**(1), 31–44 (1964)
26. M.M. Jakšić, Electrocatalysis of hydrogen evolution in the light of the brewer–engel theory for bonding in metals and intermetallic phases. *Electrochim. Acta* **29**(11), 1539–1550 (1984)
27. M.M. Jaksic, Advances in electrocatalysis for hydrogen evolution in the light of the Brewer–Engel valence-bond theory. *J. Mol. Catal.* **38**(1–2), 161–202 (1986)
28. T. Kitamura, C. Iwakura, H. Tamura, *Chem. Lett.* **5**, 965 (1981)
29. K.-I. Machida, M. Enyo, G. Adachi, H. Sakaguchi, J. Shiokawa, Electrocatalysis in metal hydride electrode. II. Hydrogen electrode reaction and related properties of group-IB metal-coated LaNi<sub>5</sub> electrodes. *Bull. Chem. Soc. Jpn.* **59**(3), 925–926 (1986)
30. M. Alsabet, M. Grden, G. Jerkiewicz, Electrochemical growth of surface oxides on nickel. Part 1: Formation of  $\alpha$ -Ni(OH)<sub>2</sub> in relation to the polarization potential, polarization time, and temperature. *Electrocatalysis* **2**(4), 317–330 (2011)
31. J.R.C. Salgado, M.H.S. Andrade, J.C.P. Silva, J. Tonholo, A voltammetric study of  $\alpha$ - and  $\beta$ -hydroxides over nickel alloys. *Electrochim. Acta* **47**(12), 1997–2004 (2002)
32. A. Baiker, H. Baris, J.H. Güntherodt, Novel hydrogenation catalyst prepared from an amorphous Cu<sub>70</sub>Zr<sub>30</sub>precursor. *J. Chem. Soc. Chem. Commun.* **12**, 930–932 (1986)
33. A. Baiker, D. Gasser, J. Lenzner, *J. Chem. Soc. Chem. Commun.* **1750** (1987)
34. H. Yamashita, M. Yoshikawa, T. Funabiki, S. Yoshida, *J. Chem. Soc. Faraday Trans.* **1**(82), 1771 (1986)
35. A. Baiker, Metallic glasses in heterogeneous catalysis. *Faraday Discuss. Chem. Soc.* **87**, 239 (1989)
36. M. Hirscher, J. Mossinger, H. Kronmuller, Hydrogen diffusion in nanocrystalline, mesoscopic, and microcrystalline heterogeneous alloys. *J. Alloys Compd.* **231**(1–2), 267–273 (1995)
37. D.S.P. Cardoso, L. Amaral, D.M.F. Santos, B. Šljukić, C.A.C. Sequeira, D. Macciò, A. Saccone, Enhancement of hydrogen evolution in alkaline water electrolysis by using nickel–rare earth alloys. *Int. J. Hydrol. Energy* **40**(12), 4295–4302 (2015)
38. G. Wu, N. Li, C.S. Dai, D.R. Zhou, Electrochemical preparation and characteristics of Ni–Co–LaNi<sub>5</sub> composite coatings as electrode materials for hydrogen evolution. *Mater. Chem. Phys.* **83**(2–3), 307–314 (2004)
39. W.C. Conner, J.L. Falconer, Spillover in Heterogeneous Catalysis. *Chem. Rev.* **95**(3), 759–788 (1995)
40. A.J. Bard, *Electrochemical Methods* (John Wiley & Sons, Hoboken, 2001)
41. M.P. Marceta Kaninski, V.M. Nikolic, G.S. Tasic, Z.L. Rakocevic, Electrocatalytic activation of Ni electrode for hydrogen production by electrodeposition of Co and V species. *Int. J. Hydrol. Energy* **34**(2), 703–709 (2009)
42. V.M. Nikolic, S.L. Maslovaro, G.S. Tasic, T.P. Brdaric, P.Z. Lausevic, B.B. Radak, M.P. Marceta Kaninski, Kinetics of hydrogen evolution reaction in alkaline electrolysis on a Ni cathode in the presence of Ni–Co–Mo based ionic activators. *Appl. Catal. B Environ.* **179**, 88–94 (2015)
43. S. Martinez, M. Metikoš-Huković, L. Valek, Electrocatalytic properties of electrodeposited Ni–15Mo cathodes for the HER in acid solutions: Synergistic electronic effect. *J. Mol. Catal. A Chem.* **245**(1–2), 114–121 (2006)
44. I. Herraiz-Cardona, E. Ortega, V. Pérez-Herranz, Impedance study of hydrogen evolution on Ni/Zn and Ni–Co/Zn stainless steel based electrodeposits. *Electrochim. Acta* **56**(3), 1308–1315 (2011)
45. B. Hirschorn, M.E. Orazem, B. Tribollet, V. Vivier, I. Frateur, M. Musiani, Constant-phase-element behavior caused by resistivity distributions in films. *J. Electrochem. Soc.* **157**(452), C452 (2010)
46. M.E. Orazem, B. Tribollet, *Electrochemical impedance spectroscopy* (John Wiley & Sons, Hoboken, 2008)
47. C.C.L. McCrory, S. Jung, J.C. Peters, T.F. Jaramillo, Benchmarking heterogeneous electrocatalysts for the oxygen evolution reaction. *J. Am. Chem. Soc.* **135**(45), 16977–16987 (2013)